Directional locking effects for active matter particles coupled to a periodic substrate

C. Reichhardt and C. J. O. Reichhardt

Theoretical Division and Center for Nonlinear Studies, Los Alamos National Laboratory, Los Alamos, New Mexico 87545, USA

Directional locking occurs when a particle moving over a periodic substrate becomes constrained to travel along certain substrate symmetry directions. Such locking effects arise for colloids and superconducting vortices moving over ordered substrates when the direction of the external drive is varied. Here we study the directional locking of run-and-tumble active matter particles interacting with a periodic array of obstacles. In the absence of an external biasing force, we find that the active particle motion locks to various symmetry directions of the substrate when the run time between tumbles is large. The number of possible locking directions depends on the array density and on the relative sizes of the particles and the obstacles. For a square array of large obstacles, the active particle only locks to the x, y, and $45°$ directions, while for smaller obstacles, the number of locking angles increases. Each locking angle satisfies $\theta = \arctan(p/q)$, where p and q are integers, and the angle of motion can be measured using the ratio of the velocities or the velocity distributions in the x and y directions. When a biasing driving force is applied, the directional locking behavior is affected by the ratio of the self-propulsion force to the biasing force. For large biasing, the behavior resembles that found for directional locking in passive systems. For large obstacles under biased driving, a trapping behavior occurs that is nonmonotonic as a function of increasing run length or increasing self-propulsion force, and the trapping diminishes when the run length is sufficiently large.

I. INTRODUCTION

In active matter systems, particles move under a self-propulsion force. Examples of active systems include swimming bacteria or self-driven colloids, and the activity often takes the form of driven diffusion or run-and-tumble dynamics [1,2]. In the absence of a substrate, these systems exhibit a rich variety of collective effects such as motility induced phase separation [3–7]. When barriers or a substrate is added, a number of behaviors arise that are distinct from what is observed for purely Brownian particles [8–14]. For example, in active matter ratchet effects, active particles interacting with some form of asymmetric barrier or obstacles undergo directed flow in the absence of dc driving, while for equilibrium or Brownian particles such ratchet effects are absent [15–19].

A growing number of studies have examined active matter systems coupled to a complex environment such as randomly disordered sites [20–29] or a periodic array of obstacles [24,30–38]. Extensive studies of passive particles on a periodic array of obstacles under diffusion [39–43] or an external drive [44–47] show that depinning phenomena, sliding phases, and different types of dynamical pattern formation appear when collective effects become important. Passive particles driven over a periodic substrate can undergo directional locking in which the motion becomes locked to certain symmetries of the lattice. Here, the direction of particle motion does not change smoothly as the angle of the external drive is rotated with respect to the substrate, but remains fixed for finite intervals of drive angle, producing steps in a plot of the direction of particle motion versus drive direction [48–60].

For a particle moving on a square lattice, the directional locking occurs when the particle moves p lattice constants in one direction and q lattice constants in the perpendicular direction, giving locking steps centered at angles of $\theta = \arctan(p/q)$. For example, $p/q = 0$ and $p/q = 1/1$ correspond to locking at $0°$ or $+45°$, while many other locking phases can appear at $|p/q| = 1/4, 1/3, 1/2, 2/3, 3/4, 2/1, 3/1$, and so forth. The number of locking steps depends on the relative radius of the obstacles and the particle. Small obstacles with a fixed lattice constant produce a devil's staircase hierachy of locking steps, with the smallest values of $|p/q|$ giving the largest step widths. If the substrate is a triangular lattice, then directional locking occurs at a different set of angles, including $30°$ and $60°$ [60,61].

Directional locking effects have been studied for vortices in type-II superconductors moving over periodic pinning arrays [48,51,55], classical electrons moving over antidot lattices [49], atomic motion on surfaces [59], and magnetic skyrmions driven over periodic landscapes [62–64]. The most studied directional locking system is colloids moving over either optical trap arrays or periodic arrays of posts. Here, the colloidal motion becomes locked to different symmetry directions of the substrate as either the effective biasing drive changes direction or the substrate itself is rotated under a fixed driving direction [50,52,53,55,57,60,61]. Similar locking effects can even arise for particles moving over quasiperiodic substrates [65,66]. The strength of the locking or width of the locking steps depends strongly on the properties of the particles such as their size, shape, and particle-substrate interactions, and as a result, directional locking acts as a powerful method for

sorting mixtures of different particle species. When one species locks to a symmetry direction and another species either does not lock or locks to a different symmetry direction, the species separate laterally over time. Such fractionation effects have been demonstrated for a number of colloidal [67–71] and other soft matter systems [72–78].

An open question is whether directional locking also occurs for active matter systems coupled to a periodic substrate. Such systems could potentially exhibit directional locking even in the absence of an externally applied biasing field. Volpe *et al.* experimentally examined active matter particles moving over a triangular lattice of posts under a biasing drive for varied activity, and found that the particles can lock to the symmetry directions of the substrate even when the external driving is not aligned with these symmetry directions [30]. More recently, Brun-Cosme-Bruny *et al.* examined swimming microalgae driven phototactically through a square array of obstacles, and found that the motion locks to certain symmetry angles [38]. These results suggest that a variety of directional locking effects should also occur for active matter systems with and without biasing drives.

In this work we examine run-and-tumble active matter disks moving through a square array of obstacles. In the absence of a biasing field, we find that for small run lengths the behavior is close to the diffusive limit and the particles explore the background in a uniform fashion; however, for long run lengths the particle motion becomes locked to specific symmetry directions of the obstacle lattice. The number of possible locking directions depends strongly on the size of the obstacles. For large obstacles, the particles lock along $\theta = 0°$, $45°$, and $90°$, while for smaller obstacles, additional locking directions appear with $\theta = \arctan(p/q)$ for integer p and q. The locking can be measured using the particle velocity distributions, which show peaks on the locking steps. As the obstacle radius increases, we find an increasing probability for the particles to become trapped by the obstacles. When there is an additional applied driving force, the net drift velocity in the driving direction has a nonmonotonic behavior as a function of the run length and the ratio of the motor force to the driving force. When the drive direction is rotated from $0°$ to $90°$, we observe a series of locking steps which are more pronounced for lower run lengths and smaller motor forces. If the motor force is made very large, then the locking steps disappear, but they can be restored by increasing the magnitude of the driving force. For large obstacles which produce a clogged state in the passive particle limit, we find that the activity can induce motion along certain substrate symmetry directions, producing a nonmonotonic mobility that depends on the direction of drive relative to the symmetry directions of the substrate.

II. SIMULATION

We consider N_d active run-and-tumble disks interacting with a square array of obstacles in a two-dimensional system of size $L \times L$. The radius of each obstacle, modeled as a short-range repulsive disk, is r_{obs}, and a is the obstacle lattice constant. The active particles are also modeled as short-range repulsive disks with radius r_a. The dynamics of active disk i is obtained by integrating the following overdamped equation of motion:

$$\alpha_d \mathbf{v}_i = \mathbf{F}_i^{dd} + \mathbf{F}_i^m + \mathbf{F}_i^{obs} + \mathbf{F}^D. \quad (1)$$

The velocity of the active particle is $\mathbf{v}_i = d\mathbf{r}_i/dt$, where $\mathbf{r}_i$ is the disk position. We set the damping constant α_d to 1.0. The disks can interact with each other via the disk-disk interaction force $\mathbf{F}_i^{dd}$ and with the obstacles via the disk-obstacle force $\mathbf{F}^{obs}$. In general, we consider the limit $N_d = 1$ of a single active particle, so the active disk-disk interactions are not important. The self-propulsion of the disk is produced by the motor force $\mathbf{F}_i^m$, a constant force of magnitude F_M that is applied in the randomly chosen direction $\hat{\mathbf{m}}_i$ for a run time of τ_l. After the run time has elapsed, a new motor force direction $\hat{\mathbf{m}}_i'$ is chosen randomly, corresponding to instantaneous reorientation, and the particle travels under the same motor force F_M in the new direction for a time τ_l before the motor force reorients again. We can add an external biasing force $\mathbf{F}^D$, which is first taken to have a fixed orientation along the x-direction with a magnitude F_D. We also consider the case where the magnitude F_D of the drive is fixed but the direction gradually rotates from $\theta_D = 0$ along the x direction to $\theta_D = 90°$ along the y direction. Here, $\mathbf{F}_D = F_D \cos(\theta_D)\hat{\mathbf{x}} + F_D \sin(\theta_D)\hat{\mathbf{y}}$. We measure the average velocity in the x-direction, $\langle V_x \rangle = \sum_{i=1}^{N_d} \mathbf{v}_i \cdot \hat{\mathbf{x}}$, and in the y-direction, $\langle V_y \rangle = \sum_{i=1}^{N_d} \mathbf{v}_i \cdot \hat{\mathbf{y}}$. We also measure the net velocity $\langle V \rangle = \sqrt{\langle V_x \rangle^2 + \langle V_y \rangle^2}$. We characterize the activity based on the distance l_r a free active particle would move in the absence of obstacles during a single run time, which we term the run length $l_r = F_M \tau_r$, as well as by the ratio of the motor to the drive force, F_M/F_D. In this work we focus on the low disk density regime where the collective effects are weak, placing the dynamics in the single particle limit. We fix the obstacle lattice constant $a = 4.0$ and the active disk radius $r_a = 0.5$, but vary the obstacle size, the motor force, the run length, and the external biasing force.

III. DIRECTIONAL LOCKING DUE TO ACTIVITY

In Fig. 1 we illustrate the obstacles, active particle, and trajectory for a system with $F_M = 0.4$ and no external biasing force. When the obstacle radius $r_{obs} = 1.35$ and the run length $l_r = 0.3$, as in Fig. 1(a), the behavior is close to the Brownian limit and the particle gradually explores the space between the obstacles while exhibiting no directional locking. In Fig. 1(b), where we have increased the run length to $l_r = 80$, the particle moves in one-dimensional (1D) trajectories that are locked along the $\pm x$, $\pm y$, and $\pm 45°$ directions. At an intermediate run length of $l_r = 5.6$ in Fig. 1(c), the particle motion is ballistic at short times but diffusive at longer times, which allows the particle to explore the entire system at a much faster rate compared to the $l_r = 0.1$ case. Here, since the persistent motion spans a distance of only about one substrate lattice constant a, there is no directional locking. Figure 1(d) illustrates a sample with a smaller $r_{obs} = 0.75$ at $l_r = 0.8$, where the motion is diffusive. When the run length is increased to $l_r = 80$, as in Fig. 1(e), directional locking occurs and the particle follows 1D paths aligned not only with $\pm x$, $\pm y$, and $\pm 45°$, but also with $\theta = \pm 26.56°$ and $\theta = \pm 71°$, corresponding to a translation by $2a$ in the x direction for every a in the y direction or a translation by a in the x direction for every $2a$ in the y direction, respectively. When the run length is
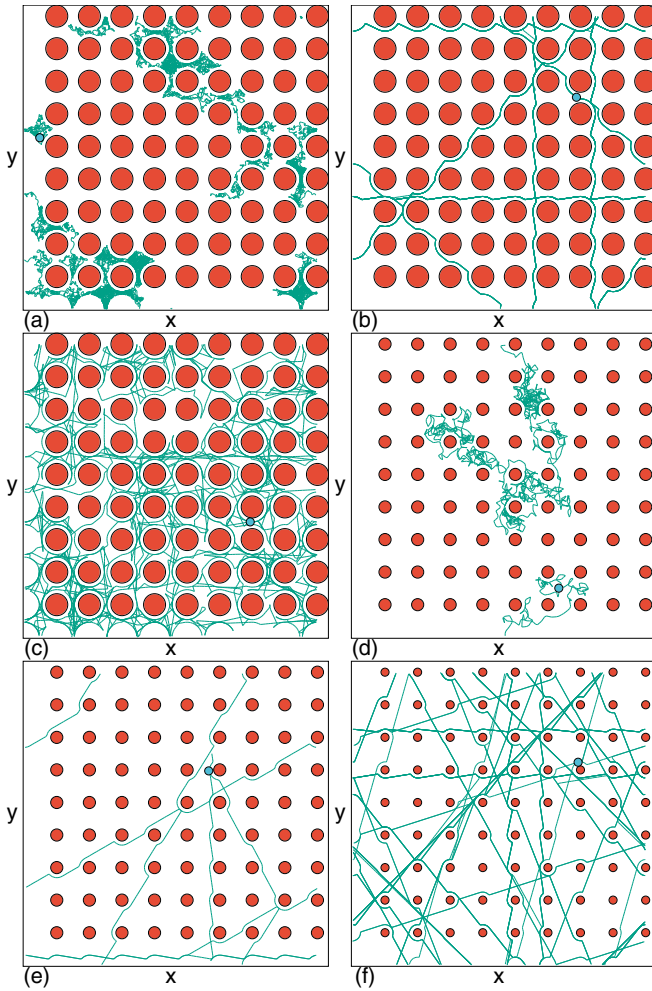
FIG. 1. Illustration of the obstacle locations (red circles), the active particle (blue circle), and the active particle trajectory (lines) in a system with motor force $F_M = 0.4$ and no external drive. (a) At obstacle radius $r_{obs} = 1.35$ and run length $l_r = 0.3$, there is no directional locking. (b) For $r_{obs} = 1.35$ and $r_l = 80$, the particle motion locks to $0°$, $45°$, and $90°$. (c) For $l_r = 5.6$ and $r_l = 80$, the motion is ballistic at short times and diffusive at long times. (d) At $r_{obs} = 0.75$ and $l_r = 0.8$, the motion is diffusive. (e) At $r_{obs} = 0.75$ and $l_r = 80$, directional locking occurs with a larger number of possible locking directions compared to panel (b). (f) At $r_{obs} = 0.5$ and $l_r = 80$, an even larger number of locking directions appear.

large, such as for $l_r = 80$, we find that as r_{obs} decreases, the number of possible locking angles increases. In Fig. 1(f) we show a sample with $l_r = 80$ and $r_{obs} = 0.5$ where the locking directions include angles for which $|p/q| = 0$, $1/1$, $1/2$, $1/3$, $1/4$, 2, 3, and 4. In general, appreciable directional locking occurs whenever the run length is larger than $2a$.

To better characterize the motion, we measure the instantaneous velocities V_x and V_y in the x and y directions along with the ratio $p/q = V_y/V_x$ which indicates the angle of the instantaneous motion. In Fig. 2(a) we plot V_x and V_y versus time for the system in Fig. 1(b) with $r_{obs} = 1.35$ and $l_r = 80$, where the particle moves in either the $\pm x$, $\pm y$, or $\pm 45°$ directions. The velocity signatures are composed of steps, with $V_x = 0$ or $V_y = 0$ when the velocity is locked along the $\pm y$ or $\pm x$
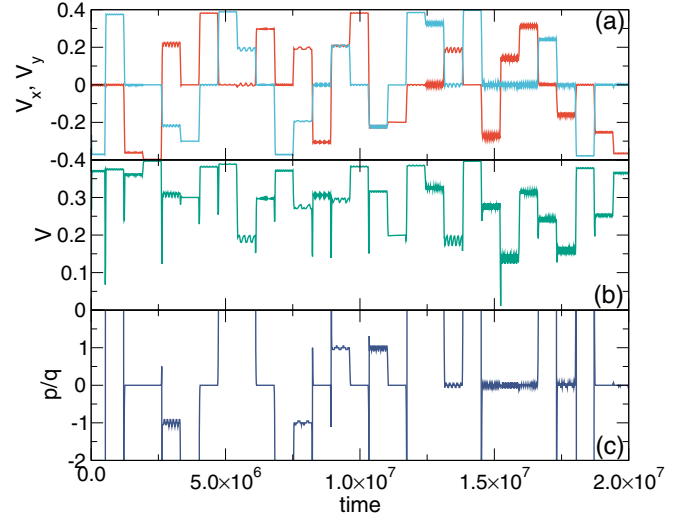

FIG. 2. (a) The instantaneous velocities in the x-direction V_x (orange) and in the y-direction V_y (light blue) versus time in simulation time steps for the system in Fig. 1(b) with $F_M = 0.4$, $r_{obs} = 1.35$, and $l_r = 80$. (b) The corresponding total velocity $V = \sqrt{V_x^2 + V_y^2}$ vs. time. (c) The corresponding $p/q = V_y/V_x$ vs. time. $p/q = \pm 1.0$ for motion along $\pm 45°$, $p/q = 0$ for motion along $\pm x$, and p/q is $\pm$ infinite for motion along $\pm y$.

direction, respectively. Since the dynamics is overdamped, we always have $|V_x| \leqslant F_M$ and $|V_y| \leqslant F_M$. In Fig. 2(b) we show the corresponding net velocity $V = \sqrt{V_x^2 + V_y^2}$ versus time. The fixed motor force might lead one to expect that $V = F_M$ at all times; however, due to collisions with the obstacles we often find $V < F_M$. When the motor force direction is aligned with a symmetry direction of the lattice, $V \approx F_M$ since few particle-obstacle collisions occur; however, if the motor force fails to align with any of the symmetry directions of the lattice, then periodic collisions occur and reduce the value of V. For example, if the motor force is aligned along $15°$, then in the absence of a substrate the particle would move at $15°$ with $V = F_M$. When the substrate is present, for the obstacle radius shown in Fig. 2 the particle motion is locked to $0°$ and the particle travels in the positive x direction, colliding regularly with the obstacles and moving at a reduced value of V. However, when the motor force is aligned along $0°$, which exactly matches a symmetry direction of the substrate, no particle-obstacle collisions occur and $V = F_M$. As a result, locked motion along a symmetry direction such as $0°$ can be associated with a range of possible net particle velocities. Figure 2(b) indicates that V generally exhibits a transient dip each time the particle changes direction due to the increased collisions that occur until the orbit stabilizes in the new locking direction. In Fig. 2(c) we plot the ratio $p/q = V_y/V_x$ versus time, which takes five distinct values: $p/q = +1.0$ for motion along $+45°$, $p/q = -1.0$ for motion along $-45°$, $p/q = 0$ for motion along $\pm x$, positive infinite p/q for motion along $+y$, and negative infinite p/q for motion along $-y$.

In Fig. 3(a) we plot V_x and V_y versus time for the system in Fig. 1(e) with $r_{obs} = 0.75$ and $l_r = 80$, while Fig. 3(b) shows the corresponding $p/q = V_y/V_x$ versus time. The velocities
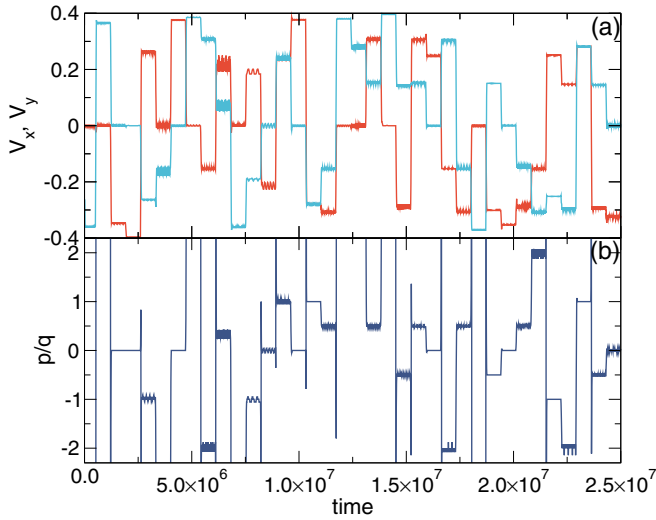
FIG. 3. (a) Instantaneous velocities V_x (orange) and V_y (light blue) vs. time in simulation time steps for the system in Fig. 1(e) with $F_M = 0.4$, $r_{obs} = 0.75$, and $l_r = 80$. (b) The corresponding $p/q = V_x/V_y$ with steps at $p/q = 0, \pm 1/2, \pm 1$, and ± 2.

again undergo a series of jumps. The smaller value of r_{obs} permits the active particle to access a larger number of symmetry directions corresponding to $p/q = 0, \pm 1/2, \pm 1$, and ± 2. In general, when l_r is large, decreasing r_{obs} increases the number of possible p/q states, as shown in Fig. 4 where we plot $|p/q|$ versus time for a system with $l_r = 80$ and a smaller $r_{obs} = 0.25$. Dashed lines highlight the locking steps that appear at $|p/q| = 0, 1/3, 1/2, 2/3, 1, 3/2, 2, 3$, and 4. For longer times beyond what is shown in Fig. 4, additional locking steps occur at $|p/q| = 1/5, 1/4, 5/2$, and 5. In general, the system spends a larger fraction of time locked along directions that correspond to lower values of p and q.

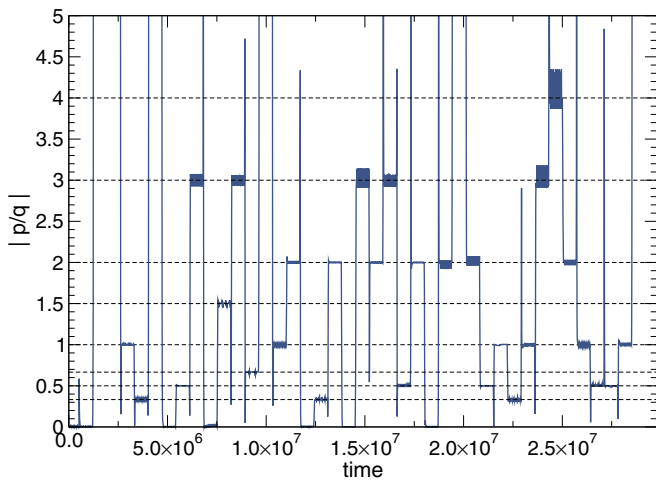For a fixed motor force and obstacle density, we can also use the distribution $P(V_x)$ of the instantaneous x velocity to

FIG. 4. The ratio $|p/q| = |V_y/V_x|$ for a system with $F_M = 0.4$, $r_{obs} = 0.25$, and $l_r = 80$. Steps appear at $|p/q| = 0, 1/3, 1/2, 2/3, 1, 3/2, 2, 3$, and 4. For longer time intervals (not shown), additional steps occur at $|p/q| = 1/5, 1/4, 5/2$, and 5.
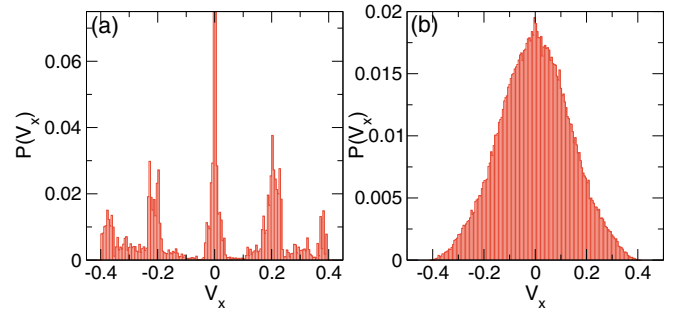

FIG. 5. The distribution $P(V_x)$ of the instantaneous x velocity for samples with $F_M = 0.4$ and $r_{obs} = 1.35$. (a) The system in Fig. 1(a) with $l_r = 80$, where the motion is locked along $\pm x$, $\pm y$, and $\pm 45°$. (b) A system with $l_r = 0.2$, where the behavior is close to Brownian motion.

characterize the system. In Fig. 5(a) we plot $P(V_x)$ for the sample from Fig. 1(a) with a long run length of $l_r = 80$, where the motion is locked to the $\pm x$, $\pm y$, or $\pm 45°$ direction, while in Fig. 5(b) we show a sample with $l_r = 0.2$ which is close to the Brownian limit. When l_r is small, $P(V_x)$ is nearly Gaussian, consistent with the expectations for a random walk. At large l_r, we find peaks in $P(V_x)$ near $V_x = \pm 0.4$ which corresponds to particles that are traveling along the $\pm x$ direction at a speed that is close to the magnitude of the motor force. A larger peak appears at $V_x = 0.0$ corresponding to motion that is locked in the $\pm y$-direction with a finite value of V_y. The $V_x = 0$ peak is not simply twice as large as either of the $V_x = \pm 0.4$ peaks, but is nearly six times higher. This is due to a trapping effect in which the particle collides with an obstacle and has an instantaneous velocity that is nearly zero. For short run lengths, a particle that has become temporarily trapped due to a collision with an obstacle quickly reorients its direction of motion and moves away, but if the run length is long, then the particles can effectively be trapped for an extended time. Such active trapping by obstacles was studied previously for run-and-tumble particles moving through random arrays under a drift force, where the active drift velocity is high at smaller l_r but drops with increasing l_r [79,80]. This trapping effect is also similar to the active particle accumulation that occurs along walls and corners when the particles persistently push up against a barrier [8,13,14,17]. Figure 5(a) also shows peaks in $P(V_x)$ near $V_x = \pm 0.22$, which corresponds to motion along $\pm 45°$. The velocity is slightly lower than the expected value of $|V_x| = F_M \cos(45°) = 0.28$ since the motor force is generally not aligned precisely along $\pm 45°$ and therefore particle-obstacle collisions occur that slow down the particle. Some additional subpeaks appear in $P(V_x)$, with the prominent peaks corresponding to additional modes of motion in which the particle collides with a quantized number of obstacles during a given time interval. The distributions shown in Fig. 5 are for a single active particle. If an increasing density of active particles is introduced, then the features in $P(V_x)$ begin to smear out due to collisions between active particles which lower the effective running length.

In Fig. 6(a) we plot $P(V_x)$ for a sample with $l_r = 80$ and a smaller obstacle size of $r_{obs} = 0.5$, which increases the number of possible locking directions. Multiple peaks appear
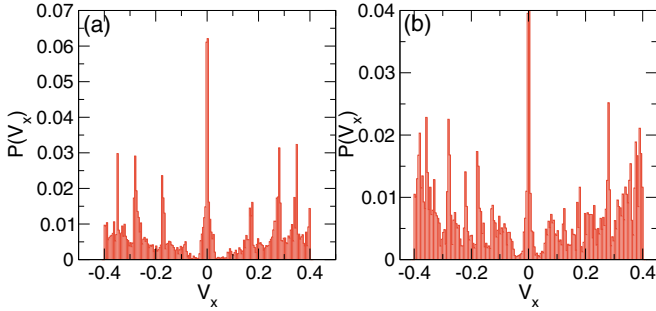
FIG. 6. $P(V_x)$ for samples with $F_M = 0.4$ and $l_r = 80$. (a) A sample with $r_{obs} = 0.5$ shows multiple peaks at $|V_x| = 0, 0.175, 0.28,$ and 0.35, corresponding to lockings of $|p/q| = 0, 1/2, 1,$ and 2. (b) A sample with $r_{obs} = 0.05$ has velocity peaks corresponding to lockings with $p/q = 0, 1/4, 1/3, 1/2, 2/3, 3/4, 1/1, 2/1, 3/1, 4/1,$ and $5/1$.

in $P(V_x)$ centered at $|V_x| = 0, 0.175, 0.28,$ and 0.35. From the relation $|V_x| = F_M \cos(\theta)$, these peaks correspond to angles of motion of $\theta = 0°, 18.43°, 45°,$ and $63.43°$, or $|p/q| = 0, 1/2, 1,$ and 2. In Fig. 6(b), a sample with $l_r = 80$ and even smaller obstacles with $r_{obs} = 0.05$ exhibits significantly more peaks corresponding to $|p/q| = 0, 1/4, 1/3, 1/2, 2/3, 3/4, 1/1, 2/1, 3/1, 4/1,$ and $5/1$.

IV. EFFECTS OF AN APPLIED BIASING FORCE

We next introduce an applied external drift force of magnitude F_D, which we initially take to have a fixed magnitude of $F_D = 0.5$ and a fixed orientation along the positive x direction, $\theta_D = 0$. In Fig. 7(a) we plot $\langle V_x \rangle / F_D$ versus F_M / F_D in a system with $r_{obs} = 1.35$ at running lengths of $l_r = 0.01, 0.1, 0.3, 1.0, 10,$ and 100. When $F_M / F_D = 0$, all of the curves coincide at $\langle V_x \rangle / F_D = 1.0$, indicating that the particle can travel freely in the x direction without hitting any obstacles. As l_r increases, $\langle V_x \rangle / F_D$ begins to decrease, with a rapid drop in $\langle V_x \rangle / F_D$ occurring once $F_M / F_D > 1.0$. This rapid drop results when the particle undergoes additional collisions with the obstacles and becomes trapped behind them for periods of time. For $l_r \geqslant 100$, $\langle V_x \rangle / F_D$ saturates to a value close to 0.725 when $F_M / F_D > 1.0$. If the obstacles are randomly placed in-
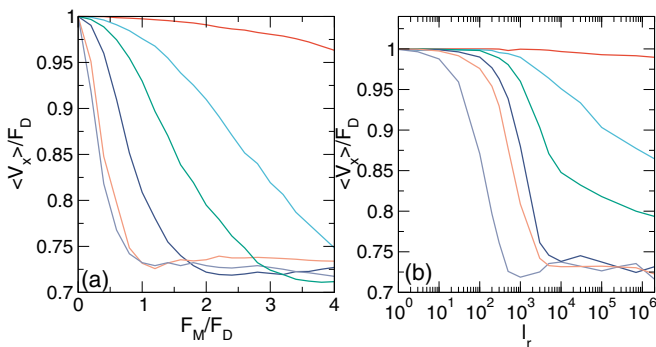

FIG. 7. $\langle V_x \rangle / F_D$ curves for a system with $r_{obs} = 1.35$ under a fixed external biasing force $F_D = 0.5$ aligned with the positive x axis. (a) $\langle V_x \rangle / F_D$ vs. F_M / F_D for running lengths $l_r = 0.01, 0.1, 0.3, 1.0, 10,$ and 100, from top to bottom. (b) $\langle V_x \rangle / F_D$ vs. l_r for $F_M / F_D = 0.04, 0.2, 0.7, 1.0,$ and 2.4, from top to bottom.
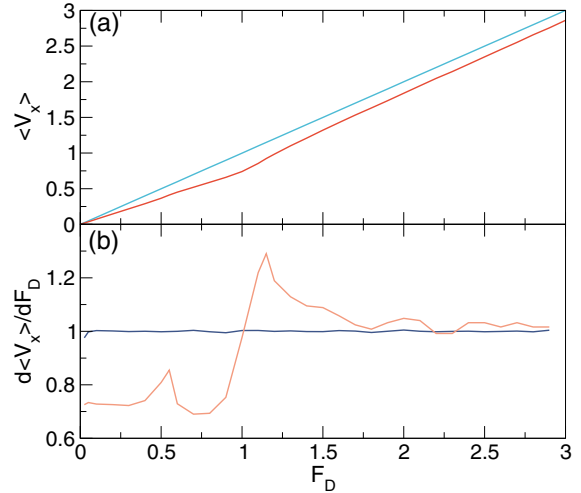

FIG. 8. (a) $\langle V_x \rangle$ vs. F_D in a system with $r_{obs} = 1.35$ and x direction driving at $F_M = 0.0$ (blue curve), showing a linear increase in $\langle V_x \rangle$ with F_D, and at $F_M = 0.5$ and $l_r = 100$ (dark orange curve). (b) The corresponding $d\langle V_x \rangle / dF_D$ curves showing no peak for the $F_M = 0.0$ system (dark blue curve) and two peaks for the $F_M = 0.4$ and $l_r = 100$ system (orange curve).

stead of being arranged in a lattice, then a similar decrease in velocity with increasing run length occurs, as previously studied in a system with a biasing force [79,80]. Figure 7(b) shows $\langle V_x \rangle / F_D$ versus run length for the system in Fig. 7(a) at $F_M / F_D = 0.04, 0.2, 0.7, 1.0,$ and 2.4. Here, $\langle V_x \rangle / F_D = 1.0$ at short run lengths and drops as l_r increases. The location of the drop shifts to lower run lengths as F_M / F_D increases.

In Fig. 8(a) we plot $\langle V_x \rangle$ versus F_D for a system with $r_{obs} = 1.35$. At $F_M = 0$, the velocity increases linearly with increasing F_D since no collisions occur between the particles and the obstacles. When $F_M = 0.5$ and $l_r = 100$, there is a reduction in $\langle V_x \rangle$ for all values of F_D since the inclusion of a motor force causes particle-obstacle collisions as well as self-trapping of the particles behind obstacles. Figure 8(b) shows the corresponding $d\langle V_x \rangle / dF_D$ versus F_D curves. When $F_M = 0.0$, $d\langle V_x \rangle / dF_D$ is flat, indicating a linear velocity-force curve, while for the finite motor force, two peaks appear in $d\langle V_x \rangle / dF_D$ near $F_D = 0.5$ and $F_D = 1.0$. At the first peak, $F_D \approx F_M$ and the motion shifts from being dominated by the motor force to being dominated by the driving force, resulting in a small upward shift of the particle velocity. The large second peak is the result of a confinement effect produced by a combination of the driving force and the periodic obstacle lattice. Particles can move freely in the interstitial channels separating the rows of obstacles, and a given particle translates by one lattice constant in the x direction in a time of approximately $\tau_o = a/F_D$. During this time, the particle also moves a distance δy in the y direction due to the motor force. If $\delta y \geqslant a/2$, then the particle can jump from one interstitial row to the next, but if $\delta y < a/2$, upon reaching the next obstacle the particle will be deflected back into its original interstitial row. When F_D is small, τ_o is large and interstitial jumping occurs frequently, producing two-dimensional motion, but as F_D increases, τ_o decreases until it is so short that the probability that $\delta y \geqslant a/2$ drops to zero. As a result, the particle motion
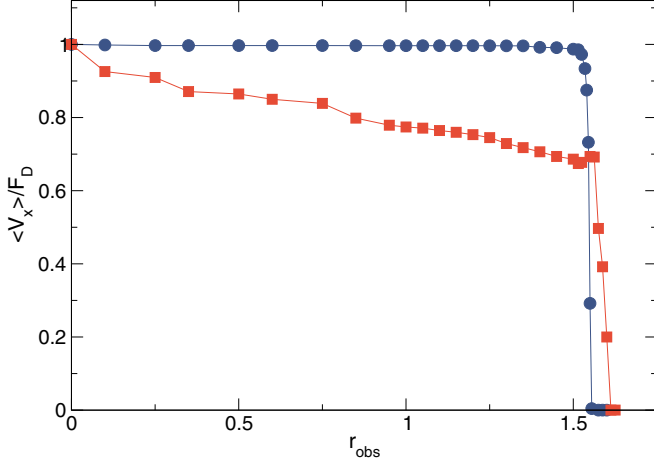
FIG. 9. $\langle V_x \rangle / F_D$ vs. r_{obs} for a system with $F_M = 0.5$ and x direction driving of $F_D = 0.2$ at $l_r = 0.01$ (blue circles) and $l_r = 10$ (orange squares). The larger run length activity lowers the overall mobility, but also increases the value of r_{obs} at which $\langle V_x \rangle / F_D$ drops to zero.

FIG. 10. $\langle V_x \rangle$ vs. θ_D for a system with $F_M = 0.5$ and $l_r = 0.01$ under a drive of $F_D = 0.5$ applied along the θ_D direction at $r_{\text{obs}} = 0.1$, 0.25, 0.5, 0.75, 1.0, 1.25, 1.35, 1.5, 1.55, 1.5625, 1.57, 1.575, 1.58, 1.5875, and 1.5925, from top (red) to bottom (purple).

becomes localized into nearly one-dimensional flow along the interstitial rows, with no jumping of particles between the rows. Thus, the second peak indicates the occurrence of a two-dimensional (2D) to 1D transition in the motion. The multiple peaks in the $d\langle V_x \rangle / dF_D$ curve are similar to the behavior typically found in a system with a depinning transition or with a transition from effectively 2D to effectively 1D dynamics [44]. For large F_D values above the second peak in $d\langle V_x \rangle / dF_D$, the system behaves in a nonactive manner.

In Fig. 9 we plot $\langle V_x \rangle / F_D$ versus r_{obs} for a system with $F_M = 0.5$ and an x direction driving force of $F_D = 0.2$ at both a small run length of $l_r = 0.01$ and a larger run length of $l_r = 10$. For the small run length, the particle velocity matches the driving velocity over most of the range of r_{obs}. Only near $r_{\text{obs}} = 1.53$ does the velocity begin to decrease precipitously until the particle becomes trapped with $\langle V_x \rangle = 0$ for $r_{\text{obs}} > 1.57$. In contrast, for the long run length $\langle V_x \rangle / F_D$ decreases with increasing r_{obs} due to the self trapping effects; however, the velocity does not drop completely to zero until $r_{\text{obs}} > 1.6$. In general, increased activity in the form of an increased run length reduces the mobility through the system; however, if strong disorder is introduced, then there can also be regimes where the higher activity increases the mobility. If the particle radius r_a is increased, then the curves for both run lengths shift to lower velocities, while the value of r_{obs} at which the velocity drops to zero decreases as $r_{\text{obs}} - r_a$.

V. DIRECTIONAL LOCKING FOR VARIED DRIVE DIRECTIONS

We next apply a finite driving force of fixed magnitude and rotate its direction from $\theta_D = 0°$ to $\theta_D = 90°$. In Fig. 10 we plot $\langle V_x \rangle$ versus θ_D for a system with $F_D = 0.5$, $F_M = 0.5$, and $l_r = 0.01$ at $r_{\text{obs}} = 0.1$, 0.25, 0.5, 0.75, 1.0, 1.25, 1.35, 1.5, 1.55, 1.5625, 1.57, 1.575, 1.58, 1.5875, and 1.5925. The velocity does not vary monotonically with θ_D but shows a series of rounded peaks which correspond to directional lock-
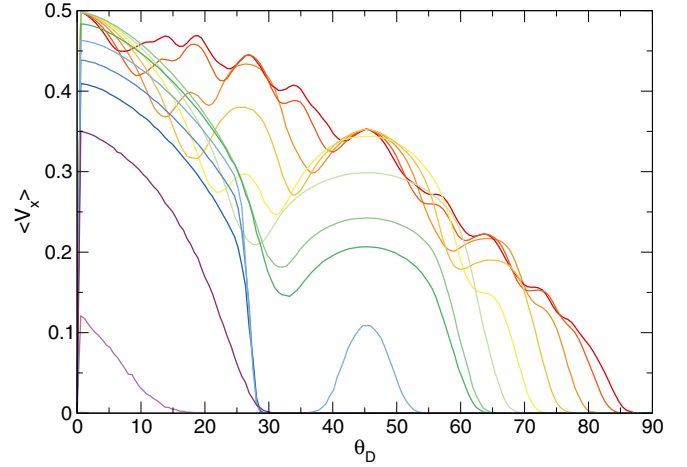
ing that would be accompanied by a series of steps in the $p/q = \langle V_y \rangle / \langle V_x \rangle$ curves. Note that directional locking in the nonactive limit $l_r = 0.0$ was studied in detail elsewhere [81]. For small $r_{\text{obs}} = 0.1$, we find steps with $p/q = 0$, 1/5, 1/4, 1/3, 1/2, 2/3, 3/4, 1/1, 4/3, 3/2, 2, 3, 4, and 5. As r_{obs} increases at small l_r, the widths of the higher order steps diminish while the steps with $p/q = 0$, 1/2, 1/1, 2/1, and y-direction locking increase in size as shown in Fig. 10. At $r_{\text{obs}} = 1.5625$, $\langle V_x \rangle$ drops to zero for $30° < \theta_D < 37°$ as well as for $\theta_D > 54°$ when the system enters a jammed or clogged state for flow that is not along x, y, or at $45°$. Above $r_{\text{obs}} = 1.57$, flow occurs only along the x or y directions, and when $r_{\text{obs}} > 1.57875$, the particle is always localized with $\langle V_x \rangle = 0$.

In Fig. 11(a) we plot $\langle V_x \rangle$ and $\langle V_y \rangle$ versus θ_D for the system in Fig. 10 at $l_r = 0.001$ and $r_{\text{obs}} = 0.1$. A series of locking steps appear, and at the $p/q = 1/1$ step, $\langle V_x \rangle = \langle V_y \rangle$. In Fig. 11(b), the same system at $l_r = 0.1$ exhibits smooth curves with no locking effects. This result indicates that increasing the activity reduces the locking effects. There is an increased likelihood that the particle can wander out of the directional locking channel before reaching the next obstacle when the correlation time of the active motor force is increased, and
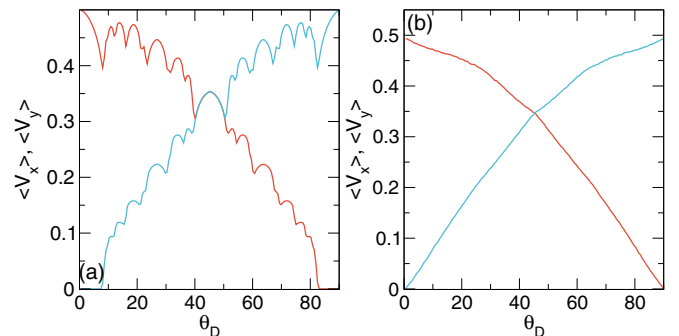

FIG. 11. $\langle V_x \rangle$ (red) and $\langle V_y \rangle$ (blue) vs. θ_D for the system in Fig. 10 with $F_M = 0.5$, $F_D = 0.5$, and $r_{\text{obs}} = 0.1$. (a) At $l_r = 0.001$, there are a series of locking steps. (b) At $l_r = 0.1$, the locking is lost.

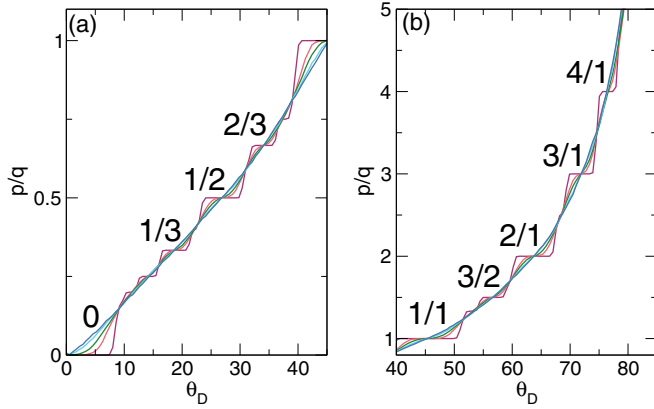FIG. 12. $p/q = \langle V_y \rangle / \langle V_x \rangle$ for the system in Fig. 11 with $F_M =$ 0.5, $F_D = 0.5$, and $r_{obs} = 0.1$ showing steps at $p/q = 0$, 1/3, 1/2, 2/3, 1/1, 3/2, 2/1, 3/1, and 4/1 for $l_r = 0.001$ (purple), 0.01 (red), 0.02 (green), 0.05 (light blue), and 0.1 (dark blue). The locking steps gradually wash out with increasing l_r. (a) The range $0° < \theta_D < 45°$. (b) The range $40° < \theta_D < 85°$.

as a result the locking effects diminish with increasing l_r. In Fig. 12 we show $p/q = \langle V_y \rangle / \langle V_x \rangle$ versus θ_D for the system in Fig. 11 at $l_r = 0.001$, 0.01, 0.02, 0.05, and 0.1, where we highlight the steps at $p/q = 0$, 1/3, 1/2, 2/3, 1/1, 3/2, 2/1, 3/1, and 4/1. As l_r increases, the locking steps gradually disappear.

For obstacles of small size, increasing the run length rapidly reduces the locking effects. Since the locking steps become wider for larger r_{obs}, we next focus on samples with $r_{obs} = 1.0$, $F_D = 0.5$ and $F_M = 0.5$, which show steps for small l_r at $p/q = 0$, 1/2, 1/1, 2/1, and for y direction locking. In Figs. 13(a) and 13(b) we plot $\langle V_x \rangle$ and $\langle V_y \rangle$ versus θ_D in this system at $l_r = 0$, 0.001, 0.003, 0.005, 0.007, 0.02, 0.03, 0.05, 0.06, 0.07, 0.08, 0.1, 0.15, 0.3, and 1.0. The locking
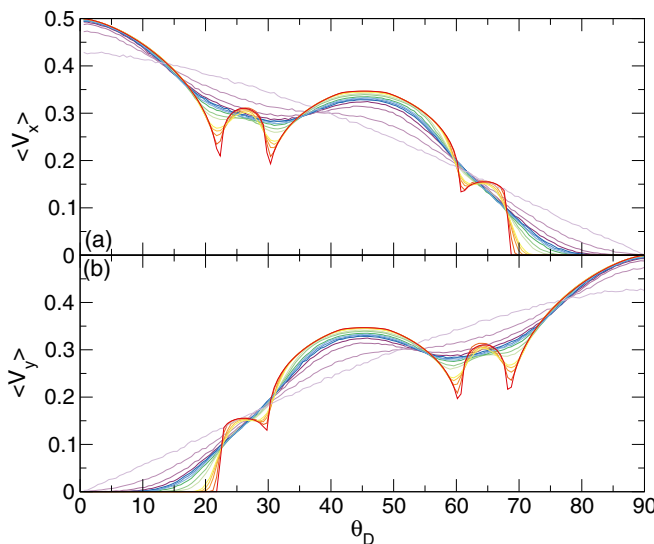

FIG. 13. (a) $\langle V_x \rangle$ and (b) $\langle V_y \rangle$ vs. θ_D for a system with $F_M = 0.5$, $F_D = 0.5$, and $r_{obs} = 1.0$ at $l_r = 0$, 0.001, 0.003, 0.005, 0. 007, 0.02, 0.03, 0.05, 0.06, 0.07, 0.08, 0.1, 0.15, 0.3, and 1.0, from bottom left (red) to top left (light purple).
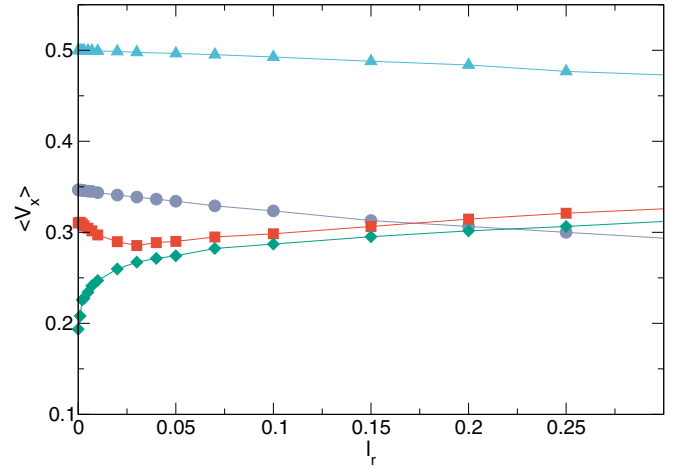

FIG. 14. $\langle V_x \rangle$ measured at specific values of θ_D vs. l_r for the system in Fig. 13 with $F_M = 0.5$, $F_D = 0.5$, and $r_{obs} = 1.0$. $\theta_D = 45°$ (purple circles), $\theta_D = 0°$ (light blue triangles), the $p/q = 1/2$ locking at $\theta_D = 26.56°$ (orange squares), and the nonlocking region at $\theta_D = 30°$ (green diamonds).

steps gradually disappear as l_r increases. The 1/2 and 2/1 steps vanish first, while the 1/1 step persists up to $l_r = 0.3$. At a specific value of θ_D, the values of $\langle V_x \rangle$ and $\langle V_y \rangle$ can decrease, increase, or show nonmonotonic behavior as a function of l_r. In Fig. 14 we plot $\langle V_x \rangle$ versus l_r at $\theta_D = 45°$ on the $p/q = 1/1$ locking step, $\theta_D = 0°$ on the $p/q = 0$ locking step, $\theta_D = 26.56°$ on the $p/q = 1/2$ locking step, and in a nonlocking region at $\theta_D = 30°$. On the $p/q = 0$ and 1/1 locking steps, $\langle V_x \rangle$ decreases monotonically with increasing l_r. For $p/q = 1/2$, $\langle V_x \rangle$ initially decreases with increasing l_r until it reaches a minimum near $l_r = 0.05$ and then increases with increasing l_r. In the nonlocking region at $\theta_D = 30°$, $\langle V_x \rangle$ monotonically increases with increasing l_r. Trends similar to those shown in Fig. 14 appear at higher l_r.

In Fig. 15(a) we plot p/q versus θ_D for the system in Fig. 13 showing that as l_r increases, the steps gradually disappear.
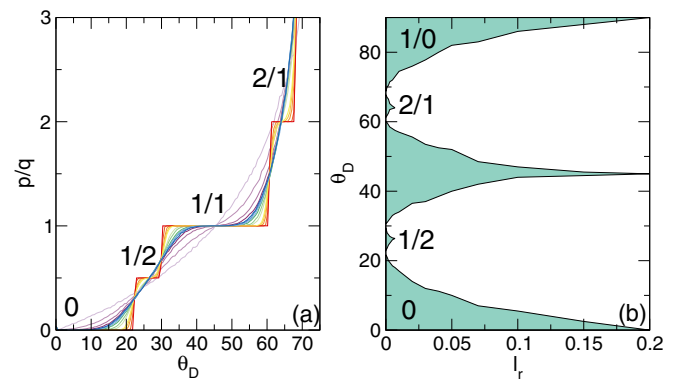

FIG. 15. (a) The evolution of p/q vs. θ_D for varied l_r for the system in Fig. 13 with $F_M = 0.5$, $F_D = 0.5$, and $r_{obs} = 1.0$ highlighting steps with $p/q = 0$, 1/2, 1/1, and 2/1. The value of l_r ranges from $l_r = 0$ (red, lower left) to $l_r = 0.2$ (pale purple, upper left). (b) The widths of the locking steps $p/q = 0$, 1/2, 1/1, 2/1, and 1/0 as a function of θ_D vs. l_r.
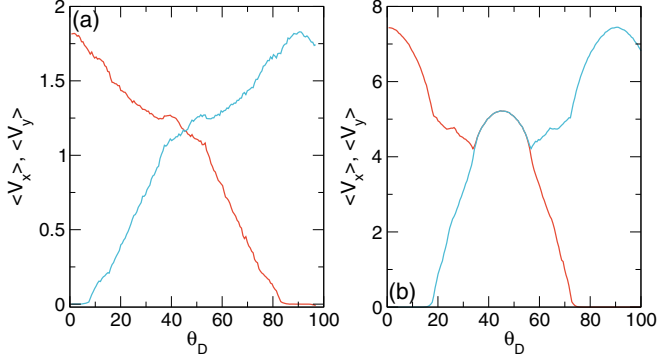
FIG. 16. $\langle V_x \rangle$ (orange) and $\langle V_y \rangle$ (light blue) versus external drive angle θ_D for a system with $F_M = 0.5$, $r_{obs} = 1.0$, and $l_r = 25$. (a) $F_D/F_M = 5.0$, where there is only a small locking window at $p/q = 1/1$. (b) $F_D/F_M = 15$, where the $p/q = 1/1$ locking window is much more extended.

This is clearest on the $p/q = 1/1$ locking step. The fact that the steps gradually vanish suggests that it would be possible to sort particles with varied run length l_r. For example, if the drive angle is set to $\theta_D = 45°$, particles with short run lengths will lock to $45°$ while particles with longer run lengths will move at an angle less than $45°$ as indicated in Fig. 14. In Fig. 15(b) we illustrate the evolution of the $p/q = 0$, $1/2$, $1/1$, $2/1$, and y direction locking steps as l_r increases. The $p/q = 1/2$ and $2/1$ locking steps disappear when $l_r > 0.03$, while the other locking steps persist up to $l_r = 0.2$. Partial locking (not shown) persists up to $l_r = 0.3$. For larger r_{obs}, the locking phases for $p/q = 0$, $1/1$ and y direction locking extend out to higher values of l_r.

A. Effect of applied driving force magnitude

We next consider a system in which both the direction and the magnitude of the external biasing force are varied while the motor force magnitude F_M is held fixed. We consider a range of values from the motor force dominated regime with $F_D/F_M \leqslant 1.0$ to the external biasing force dominated regime with $F_D/F_M > 1.0$. As shown in the previous section, when $F_D/F_M \approx 1.0$ the directional locking effects disappear for $l_r \geqslant 1.0$. We consider samples with $F_M = 0.5$ and $l_r = 25$, a combination which produces no locking in any direction when $F_D/F_M < 2.0$. In Fig. 16(a) we plot $\langle V_x \rangle$ and $\langle V_y \rangle$ at $F_D/F_M = 5.0$, where locking in x and y appears in only a small region with $p/q = 1/1$. At $F_D/F_M = 15$ in Fig. 16(b), an extended $p/q = 1/1$ locking region appears over which $\langle V_x \rangle = \langle V_y \rangle$. In Fig. 17(a) we plot p/q versus θ_D for the system in Fig. 16 at $F_D/F_M = 17$, 15, 13, 11, 9, 7, 6, 5, 4, and 3.0, highlighting the $p/q = 0/1$ and $1/1$ locking steps. For $F_D/F_M = 3.0$, there is almost no locking at $p/q = 0/1$ and no locking at $p/q = 1/1$, while for $F_D/F_M = 4.0$, weak locking appears at $p/q = 0/1$ but there is still no locking at $p/q = 1/1$. As F_D/F_M increases, the $p/q = 1/1$ locking step emerges and becomes wider, and indications of partial locking appear near $p/q = 1/4$ and $p/q = 1/2$. In Fig. 17(b) we plot the total velocity $\langle V \rangle$ versus θ_D for the same system at $F_D/F_M = 17$, 15, 13, 11, 9, 7, 6, 5, 4, 3, 2, 1.5, and 1. As F_D/F_M increases, the net velocity increases, and strong oscillations emerge in
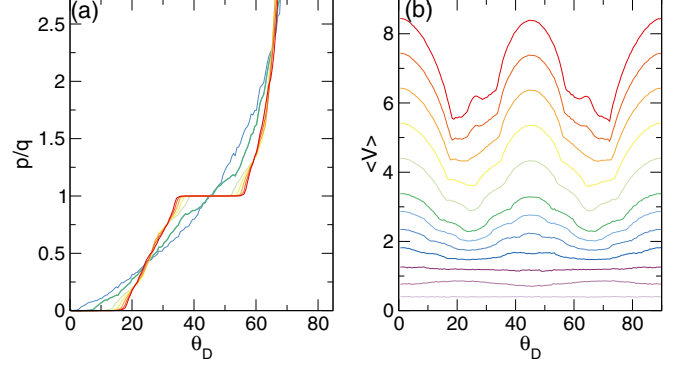

FIG. 17. (a) p/q vs. θ_D for a system with $F_M = 0.5$, $r_{obs} = 1.0$, and $l_r = 25$ at $F_D/F_M = 17$ (red), 15, 13, 11, 9, 7, 6, 5, 4, and 3 (blue), from lower left to upper left, showing that the $p/q = 1/1$ step disappears as F_M/F_D decreases. (b) $\langle V \rangle$ vs. θ_D in the same system at $F_D/F_M = 17$ (red), 15, 13, 11, 9, 7, 6, 5, 4, 3, 2, 1.5, and 1 (light purple), from top to bottom.

$\langle V \rangle$ so that the locking steps at $p/q = 0/1$, $1/1$, and y direction locking appear as clear bumps. For $F_D/F_M = 17$ and 15, there are smaller bumps near $\theta = 26°$ and $65°$, corresponding to $p/q = 1/2$ and $p/q = 3/2$; however, this locking is only partial. For $F_D/F_M = 1.0$, $\langle V \rangle$ does not depend on θ_D, indicating the absence of full or partial locking. In Fig. 18 we plot the locations of the $p/q = 0$, $1/1$, and $1/0$ steps as a function of θ_D versus F_D/F_M, showing that locking effects occur only when $F_D/F_M > 2.0$. These results indicate that even for very long run lengths, directional locking can occur as long as the external biasing force is at least twice as large as the motor force. This suggests that particles that couple differently to the external drive could be separated, with slow moving active particles following the direction of the external drive and fast moving active particles locking to one of the different symmetry directions.
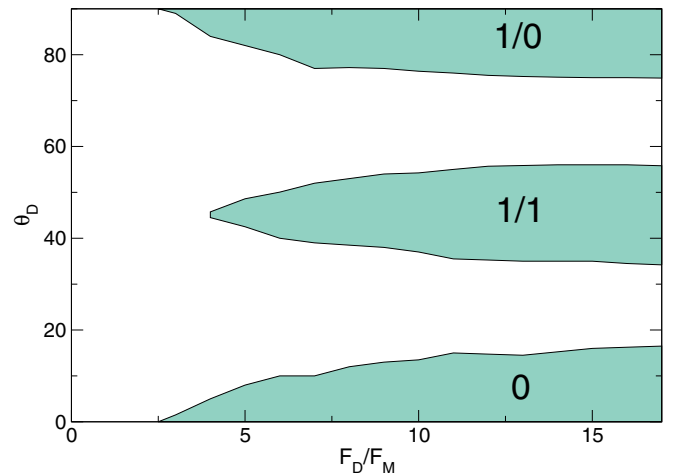

FIG. 18. Locations of the $p/q = 0$, $1/1$, and $1/0$ steps as a function of θ_D versus F_D/F_M for a system with $F_M = 0.5$, $r_{obs} = 1.0$, and $l_r = 25$.
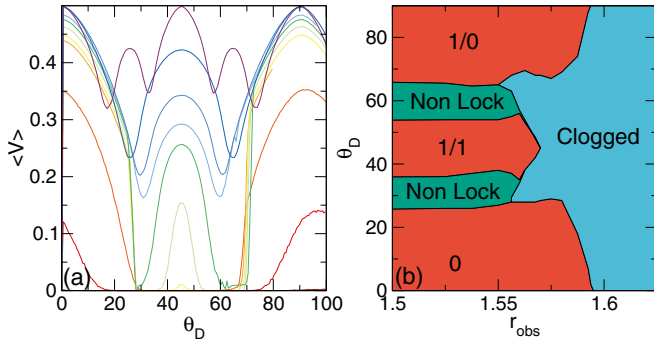
FIG. 19. (a) The total velocity $\langle V \rangle$ vs. θ_D for a system with $F_D = 0.5$, $F_M = 0.5$, and $l_r = 0.01$ for $r_{obs} = 0.75$, 1.25, 1.5, 1.55, 1.556, 1.562, 1.5675, 1.57, 1.58, 1.5875, and 1.5925, from center top (purple) to center bottom (red). (b) Dynamic phase diagram as a function of θ_D vs. r_{obs} for the system in (a) with $r_{obs} > 1.5$, showing the locations of the $p/q = 0$, 1/1, and 1/0 locking steps, nonlocking regimes, and the clogged state.

B. Clogging effects

We next consider large obstacles which can induce clogging effects depending on the level of activity in the systems. In Fig. 19(a) we plot the total velocity $\langle V \rangle$ versus θ_D for a system with $F_D = 0.5$, $F_M = 0.5$, and $l_r = 0.01$ at $r_{obs} = 0.75$, 1.25, 1.5, 1.55, 1.556, 1.562, 1.5675, 1.57, 1.58, 1.5875, and 1.5925. For $r_{obs} = 0.75$, locking steps appear at $p/q = 0$, 1/2, 1/1, 3/2, and y direction locking. As r_{obs} increases, the net velocity decreases. When $r_{obs} < 1.562$, $\langle V \rangle$ drops to zero for driving in certain directions but locking steps are still present for $\theta_D = 0°$, 45°, and 90°, while for $r_{obs} > 1.57$ locking occurs only along the x and y directions. At large enough r_{obs}, the system becomes completely clogged. In Fig. 19(b) we show a dynamic phase diagram for the system in Fig. 19(a) in the regime $r_{obs} > 1.5$, where we highlight the $p/q = 1/1$ and 1/0 locked phases, regions where unlocked flow occurs, and the clogged state. The clogging regions interdigitate with the non-locking regions, indicating that there is a higher susceptibility to clogging for driving at certain nonlocking angles. For the larger obstacle sizes, the system is always clogged.

The tendency for a system with a periodic array of obstacles to clog for driving in different directions was previously studied for passive bidisperse disks in Ref. [82]. Even when free flow of the disks is possible along the x or y directions, the system can clog for driving at incommensurate angles due to collisions between the disks and the obstacles. For a square obstacle array, the disks can move without collisions for driving along 45°; however, the effective distance between the obstacles is smaller compared to driving in the x or y directions, so the system reaches a clogged state at lower r_{obs} for the 45° driving compared to x or y driving. In the active particle system we consider here, the clogging is a single particle effect that is produced by the interplay between the drive force, the motor force, and the disk-obstacle interactions. For a disk-obstacle interaction with a softer form, the onset of clogging shifts to larger values of r_{obs}, whereas if F_D or F_M are reduced, then the clogging onset shifts to smaller values of r_{obs}. The amount of clogging that occurs for a fixed drive and motor force also depends on the size of l_r. If collective
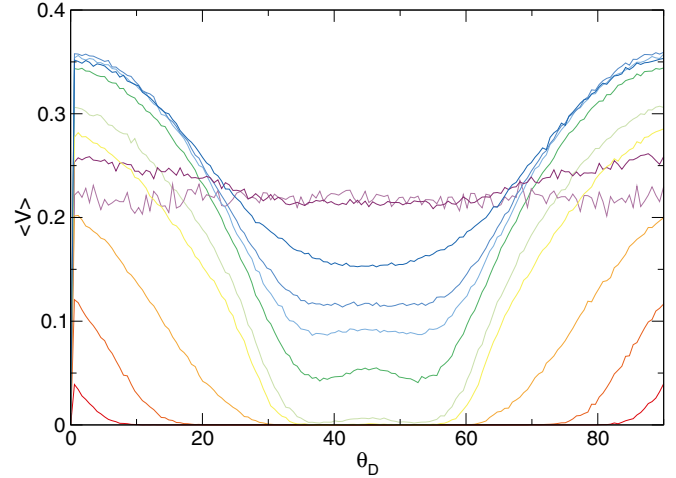

FIG. 20. $\langle V \rangle$ vs. θ_D for the system in Fig. 19 with $F_D = 0.5$, $F_M = 0.5$, and $r_{obs} = 1.5875$ at $l_r = 0.005$, 0.01, 0.03, 0.07, 0.1, 0.2, 0.3, 0.4, 0.7, 5, and 25, from center bottom (red) to center top (light purple).

particle-particle interactions become important, then distinct types of jamming or clogging effects [83–86] could arise that differ from what we observe. The activity could reduce clogging effects at small run lengths, but could increase the clogging or induce partial clogging for large run lengths, as shown in studies of active particles driven through randomly placed obstacles [22,25].

In Fig. 20 we plot $\langle V \rangle$ versus θ_D for the system in Fig. 19 at $r_{obs} = 1.5875$ for $l_r = 0.005$, 0.01, 0.03, 0.07, 0.1, 0.2, 0.3, 0.4, 0.7, 5, and 25. Increasing the run length produces a variety of effects. At $\theta_D = 0°$, $\langle V \rangle$ gradually increases with increasing l_r until reaching the value $\langle V \rangle = 0.355$ near $l_r = 0.7$. As l_r is increased further, $\langle V \rangle$ decreases to $\langle V \rangle = 0.21$ due to a self-trapping effect. At $\theta_D = 45°$, $\langle V \rangle$ monotonically increases with increasing r_l and the clogging effect disappears entirely for $l_r > 0.1$. If r_{obs} is increased, then the value of l_r at which an unclogged state appears increases. A local maximum in
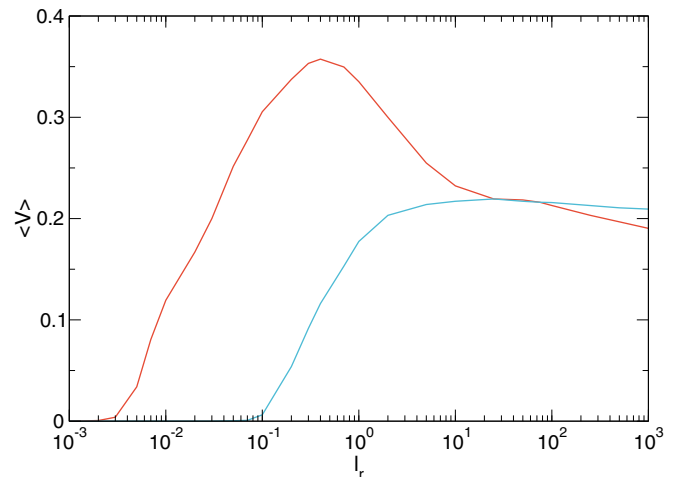

FIG. 21. $\langle V \rangle$ vs. l_r at $\theta_D = 0$ (orange) and $\theta_D = 45°$ (blue) for the system in Fig. 20 with $F_D = 0.5$, $F_M = 0.5$, and $r_{obs} = 1.5875$.

$\langle V \rangle$ appears at $\theta_D = 45°$ when $l_r = 0.1$, 0.2, and 0.3 due to a partial locking to the $p/q = 1/1$ step. These results suggest that active particle sorting could be achieved using clogging effects in which the less active particles with shorter run lengths would be trapped but the more active particles with longer run lengths would be mobile.

In Fig. 21 we plot $\langle V \rangle$ versus l_r for the system in Fig. 20 at $\theta_D = 0°$ and $\theta = 45°$. For $l_r < 0.01$, the system is completely clogged. When $l_r \geqslant 0.01$, $\langle V \rangle$ for $\theta_D = 0°$ increases with increasing l_r to a maximum value near $l_r = 1.0$, after which $\langle V \rangle$ decreases with increasing l_r. At $\theta_D = 45°$, the sample is clogged below $l_r = 0.5$. There is then an increase in $\langle V \rangle$ with increasing l_r up to a maximum value near $l_r = 100$, followed by a slight decrease in $\langle V \rangle$.

VI. SUMMARY

We have examined active run-and-tumble particles interacting with a square array of obstacles. For a system without any external biasing, we find that for short run times the particles act close to the Brownian limit and explore space randomly. For long run times, the particles become directionally locked and move only along certain symmetry directions of the substrate. These directions correspond to angles $\theta = \arctan(p/q)$ where p and q are integers. As the radius of the obstacles increases, the number of locking angles decreases

until only the steps at $p/q = 0$, $p/q = 1/1$, and y direction locking remain. The locking can be measured by examining the ratio of the x and y direction velocities as well as the instantaneous velocity distribution functions. When an additional biasing drive is applied in the x direction, the average drift velocity decreases if the run time is increased, while an increase in the magnitude of the external biasing force relative to the motor force can produce peaks in the differential velocity-force curves. As the direction of the external drive is changed, we observe a directional locking effect similar to that found in nonactive systems. Increasing the run time destroys the directional locking, but if the ratio of the biasing driving force to the motor force is made large enough, then the directional locking reappears. For large obstacles, the system can exhibit a directional depinning and clogging effect in which increasing the run time can induce the onset of clogging.

[1] M. C. Marchetti, J. F. Joanny, S. Ramaswamy, T. B. Liverpool, J. Prost, M. Rao, and R. A. Simha, Hydrodynamics of soft active matter, Rev. Mod. Phys. **85**, 1143 (2013).

[2] C. Bechinger, R. Di Leonardo, H. Löwen, C. Reichhardt, G. Volpe, and G. Volpe, Active particles in complex and crowded environments, Rev. Mod. Phys. **88**, 045006 (2016).

[3] Y. Fily and M. C. Marchetti, Athermal Phase Separation of Self-Propelled Particles with No Alignment, Phys. Rev. Lett. **108**, 235702 (2012).

[4] G. S. Redner, M. F. Hagan, and A. Baskaran, Structure and Dynamics of a Phase-Separating Active Colloidal Fluid, Phys. Rev. Lett. **110**, 055701 (2013).

[5] M. E. Cates and J. Tailleur, Motility-induced phase separation, Ann. Rev. Condens. Matter Phys. **6**, 219 (2015).

[6] J. Palacci, S. Sacanna, A. P. Steinberg, D. J. Pine, and P. M. Chaikin, Living crystals of light-activated colloidal surfers, Science **339**, 936 (2013).

[7] I. Buttinoni, J. Bialké, F. Kümmel, H. Löwen, C. Bechinger, and T. Speck, Dynamical Clustering and Phase Separation in Suspensions of Self-Propelled Colloidal Particles, Phys. Rev. Lett. **110**, 238301 (2013).

[8] X. Yang, M. L. Manning, and M. C. Marchetti, Aggregation and segregation of confined active particles, Soft Matter **10**, 6477 (2014).

[9] S. A. Mallory, C. Valeriani, and A. Cacciuto, Curvature-induced activation of a passive tracer in an active bath, Phys. Rev. E **90**, 032309(R) (2014).

[10] S. C. Takatori, W. Yan, and J. F. Brady, Swim Pressure: Stress Generation in Active Matter, Phys. Rev. Lett. **113**, 028103 (2014).

[11] D. Ray, C. Reichhardt, and C. J. Olson Reichhardt, Casimir effect in active matter systems, Phys. Rev. E **90**, 013019 (2014).

[12] R. Ni, M. A. Cohen Stuart, and P. G. Bolhuis, Tunable Long Range Forces Mediated by Self-Propelled Colloidal Hard Spheres, Phys. Rev. Lett. **114**, 018302 (2015).

[13] A. P. Solon, Y. Fily, A. Baskaran, M. E. Cates, Y. Kafri, M. Kardar, and J. Tailleur, Pressure is not a state function for generic active fluids, Nature Phys. **11**, 673 (2015).

[14] T. Speck, Collective forces in scalar active matter, Soft Matter **16**, 2652 (2020).

[15] M. B. Wan, C. J. Olson Reichhardt, Z. Nussinov, and C. Reichhardt, Rectification of Swimming Bacteria and Self-Driven Particle Systems by Arrays of Asymmetric Barriers, Phys. Rev. Lett. **101**, 018102 (2008).

[16] N. Nikola, A. P. Solon, Y. Kafri, M. Kardar, J. Tailleur, and R. Voituriez, Active Particles with Soft and Curved Walls: Equation of State, Ratchets, and Instabilities, Phys. Rev. Lett. **117**, 098001 (2016).

[17] C. J. Olson Reichhardt and C. Reichhardt, Ratchet effects in active matter systems, Ann. Rev. Condens. Matter Phys. **8**, 51 (2017).

[18] I. Berdakin, Y. Jeyaram, V. V. Moshchalkov, L. Venken, S. Dierckx, S. J. Vanderleyden, A. V. Silhanek, C. A. Condat, and V. I. Marconi, Influence of swimming strategy on microorganism separation by asymmetric obstacles, Phys. Rev. E **87**, 052702 (2013).

[19] C. Lozano, B. ten Hagen, H. Löwen, and C. Bechinger, Phototaxis of synthetic microswimmers in optical landscapes, Nature Commun. **7**, 12828 (2016).

[20] O. Chepizhko and F. Peruani, Active particles in heterogeneous media display new physics, Eur. Phys. J. Spec. Top. **224**, 1287 (2015).

[21] A. Morin, N. Desreumaux, J.-B. Caussin, and D. Bartolo, Distortion and destruction of colloidal flocks in disordered environments, Nature Phys. **13**, 63 (2017).

[22] Cs. Sándor, A. Libál, C. Reichhardt, and C. J. Olson Reichhardt, Dynamic phases of active matter systems with quenched disorder, Phys. Rev. E **95**, 032606(R) (2017).

[23] A. Morin, D. Lopes Cardozo, V. Chikkadi, and D. Bartolo, Diffusion, subdiffusion, and localization of active colloids in random post lattices, Phys. Rev. E **96**, 042611 (2017).

[24] M. Zeitz, K. Wolff, and H. Stark, Active Brownian particles moving in a random Lorentz gas, Eur. Phys. J. E **40**, 23 (2017).

[25] C. Reichhardt and C. J. O. Reichhardt, Clogging and depinning of ballistic active matter systems in disordered media, Phys. Rev. E **97**, 052613 (2018).

[26] T. Bertrand, Y. Zhao, O. Bénichou, J. Tailleur, and R. Voituriez, Optimized Diffusion of Run-and-Tumble Particles in Crowded Environments, Phys. Rev. Lett. **120**, 198103 (2018).

[27] O. Chepizhko and T. Franosch, Ideal circle microswimmers in crowded media, Soft Matter **15**, 452 (2019).

[28] T. Bhattacharjee and S. S. Datta, Confinement and activity regulate bacterial motion in porous media, Soft Matter **15**, 9920 (2019).

[29] A. Chardac, S. Shankar, M. C. Marchetti, and D. Bartolo, Meandering flows and dynamical vortex glasses in disordered polar active matter, arXiv:2002.12893.

[30] G. Volpe, I. Buttinoni, D. Vogt, H.-J. Kümmerer, and C. Bechinger, Microswimmers in patterned environments, Soft Matter **7**, 8810 (2011).

[31] D. A. Quint and A. Gopinathan, Topologically induced swarming phase transition on a 2D percolated lattice, Phys. Biol. **12**, 046008 (2015).

[32] R. Alonso-Matilla, B. Chakrabarti, and D. Saintillan, Transport and dispersion of active particles in periodic porous media, Phys. Rev. Fluids **4**, 043101 (2019).

[33] T. Jakuszeit, O. A. Croze, and S. Bell, Diffusion of active particles in a complex environment: Role of surface scattering, Phys. Rev. E **99**, 012610 (2019).

[34] S. Pattanayak, R. Das, M. Kumar, and S. Mishra, Enhanced dynamics of active Brownian particles in periodic obstacle arrays and corrugated channels, Eur. Phys. J. E **42**, 62 (2019).

[35] K. Schakenraad, L. Ravazzano, N. Sarkar, J. A. J. Wondergem, R. M. H. Merks, and L. Giomi, Topotaxis of active Brownian particles, Phys. Rev. E **101**, 032602 (2020).

[36] H. E. Ribeiro, W. P. Ferreira, and Fabrício Q. Potiguar, Trapping and sorting of active matter in a periodic background potential, Phys. Rev. E **101**, 032126 (2020).

[37] S. Yazdi, J. L. Aragones, J. Coulter, and A. Alexander-Katz, Metamaterials for active colloid transport, arXiv:2002.06477.

[38] M. Brun-Cosme-Bruny, A. Förtsch, W. Zimmermann, E. Bertin, P. Peyla, and S. Rafaï, Deflection of phototactic microswimmers through obstacle arrays, Phys. Rev. Fluids **5**, 093302 (2020).

[39] M. Brunner and C. Bechinger, Phase Behavior of Colloidal Molecular Crystals on Triangular Light Lattices, Phys. Rev. Lett. **88**, 248302 (2002).

[40] K. Mangold, P. Leiderer, and C. Bechinger, Phase Transitions of Colloidal Monolayers in Periodic Pinning Arrays, Phys. Rev. Lett. **90**, 158302 (2003).

[41] C. Reichhardt and C. J. Olson Reichhardt, Ordering and melting in colloidal molecular crystal mixtures, Phys. Rev. E **71**, 062403 (2005).

[42] A. M. Lacasta, J. M. Sancho, A. H. Romero, I. M. Sokolov, and K. Lindenberg, From subdiffusion to superdiffusion of particles on solid surfaces, Phys. Rev. E **70**, 051104 (2004).

[43] S. Herrera-Velarde and R. Castañeda Priego, Diffusion in two-dimensional colloidal systems on periodic substrates, Phys. Rev. E **79**, 041407 (2009).

[44] C. Reichhardt and C. J. Olson Reichhardt, Depinning and nonequilibrium dynamic phases of particle assemblies driven over random and ordered substrates: A review, Rep. Prog. Phys. **80**, 026501 (2017).

[45] T. Bohlein, J. Mikhael, and C. Bechinger, Observation of kinks and antikinks in colloidal monolayers driven across ordered surfaces, Nature Mater. **11**, 126 (2012).

[46] A. Vanossi, N. Manini, and E. Tosatti, Static and dynamic friction in sliding colloidal monolayers, Proc. Natl. Acad. Sci. USA **109**, 16429 (2012).

[47] D. McDermott, J. Amelang, C. J. Olson Reichhardt, and C. Reichhardt, Dynamic regimes for driven colloidal particles on a periodic substrate at commensurate and incommensurate fillings, Phys. Rev. E **88**, 062301 (2013).

[48] C. Reichhardt and F. Nori, Phase Locking, Devil's Staircases, Farey Trees, and Arnold Tongues in Driven Vortex Lattices with Periodic Pinning, Phys. Rev. Lett. **82**, 414 (1999).

[49] J. Wiersig and K.-H. Ahn, Devil's Staircase in the Magnetoresistance of a Periodic Array of Scatterers, Phys. Rev. Lett. **87**, 026803 (2001).

[50] P. T. Korda, M. B. Taylor, and D. G. Grier, Kinetically Locked-in Colloidal Transport in an Array of Optical Tweezers, Phys. Rev. Lett. **89**, 128301 (2002).

[51] A. V. Silhanek, L. Van Look, S. Raedts, R. Jonckheere, and V. V. Moshchalkov, Guided vortex motion in superconductors with a square antidot array, Phys. Rev. B **68**, 214504 (2003).

[52] A. Gopinathan and D. G. Grier, Statistically Locked-in Transport through Periodic Potential Landscapes, Phys. Rev. Lett. **92**, 130602 (2004).

[53] M. Balvin, E. Sohn, T. Iracki, G. Drazer, and J. Frechette, Directional Locking and the Role of Irreversible Interactions in Deterministic Hydrodynamics Separations in Microfluidic Devices, Phys. Rev. Lett. **103**, 078301 (2009).

[54] J. Koplik and G. Drazer, Nanoscale simulations of directional locking, Phys. Fluids **22**, 052005 (2010).

[55] C. Reichhardt and C. J. Olson Reichhardt, Structural transitions and dynamical regimes for directional locking of vortices and colloids driven over periodic substrates, J. Phys.: Condens. Matter **24**, 225702 (2012).

[56] X. Li, C. Wu, T. Cao, and Y. Cao, Directional mode-locking of driven two-dimensional active magnetized colloids with periodic pinning centers, Physica A **515**, 279 (2019).

[57] P. Tierno, A moire foray, Nature Phys. **15**, 733 (2019).

[58] X. Cao, E. Panizon, A. Vanossi, N. Manini, and C. Bechinger, Orientational and directional locking of colloidal clusters driven across periodic surfaces, Nature Phys. **15**, 776 (2019).

[59] F. Trillitzsch, R. Guerra, A. Janas, N. Manini, F. Krok, and E. Gnecco, Directional and angular locking in the driven motion of Au islands on MoS$_2$, Phys. Rev. B **98**, 165417 (2018).

[60] R. L. Stoop, A. V. Straube, T. H. Johansen, and P. Tierno, Collective Directional Locking of Colloidal Monolayers on a Periodic Substrate, Phys. Rev. Lett. **124**, 058002 (2020).

[61] C. Reichhardt and C. J. Olson Reichhardt, Directional locking effects and dynamics for particles driven through a colloidal lattice, Phys. Rev. E **69**, 041405 (2004).

[62] C. Reichhardt, D. Ray, and C. J. Olson Reichhardt, Quantized transport for a skyrmion moving on a two-dimensional periodic substrate, Phys. Rev. B **91**, 104426 (2015).

[63] J. Feilhauer, S. Saha, J. Tobik, M. Zelent, L. J. Heyderman, and M. Mruczkiewicz, Controlled motion of skyrmions in a magnetic antidot lattice, arXiv:1910.07388.

[64] N. P. Vizarim, C. Reichhardt, C. J. O. Reichhardt, and P. A. Venegas, Skyrmion dynamics and topological sorting on periodic obstacle arrays, New J. Phys. **22**, 053025 (2020).

[65] C. Reichhardt and C. J. Olson Reichhardt, Dynamical Ordering and Directional Locking for Particles Moving over Quasicrystalline Substrates, Phys. Rev. Lett. **106**, 060603 (2011).

[66] T. Bohlein and C. Bechinger, Experimental Observation of Directional Locking and Dynamical Ordering of Colloidal Monolayers Driven Across Quasiperiodic Substrates, Phys. Rev. Lett. **109**, 058301 (2012).

[67] M. P. MacDonald, G. C. Spalding, and K. Dholakia, Microfluidic sorting in an optical lattice, Nature (London) **426**, 421 (2003).

[68] M. Pelton, K. Ladavac, and D. G. Grier, Transport and fractionation in periodic potential-energy landscapes, Phys. Rev. E **70**, 031108 (2004).

[69] K. Ladavac, K. Kasza, and D. G. Grier, Sorting mesoscopic objects with periodic potential landscapes: Optical fractionation, Phys. Rev. E **70**, 010901(R) (2004).

[70] A. M. Lacasta, J. M. Sancho, A. H. Romero, and K. Lindenberg, Sorting on Periodic Surfaces, Phys. Rev. Lett. **94**, 160601 (2005).

[71] Y. Roichman, V. Wong, and D. G. Grier, Colloidal transport through optical tweezer arrays, Phys. Rev. E **75**, 011407 (2007).

[72] L. R. Huang, E. C. Cox, R. H. Austin, and J. C. Sturm, Continuous particle separation through deterministic lateral displacement, Science **304**, 987 (2004).

[73] B. R. Long, M. Heller, J. P. Beech, H. Linke, H. Bruus, and J. O. Tegenfeldt, Multidirectional sorting modes in deterministic lateral displacement devices, Phys. Rev. E **78**, 046304 (2008).

[74] D. Speer, R. Eichhorn, and P. Reimann, Exploiting Lattice Potentials for Sorting Chiral Particles, Phys. Rev. Lett. **105**, 090602 (2010).

[75] S. R. Risbud and G. Drazer, Directional locking in deterministic lateral-displacement microfluidic separation systems, Phys. Rev. E **90**, 012302 (2014).

[76] B. H. Wunsch, J. T. Smith, S. M. Gifford, C. Wang, M. Brink, R. L. Bruce, R. H. Austin, G. Stolovitzky, and Y. Astier, Nanoscale lateral displacement arrays for the separation of exosomes and colloids down to 20 nm, Nat. Nanotechnol. **11**, 936 (2016).

[77] T. S. H. Tran, B. D. Ho, J. P. Beech, and Jonas O. Tegenfeldt, Open channel deterministic lateral displacement for particle and cell sorting, Lab Chip **17**, 3592 (2017).

[78] Y. Li, H. Zhang, Y. Li, X. Li, J. Wu, S. Qian, and F. Li, Dynamic control of particle separation in deterministic lateral displacement separator with viscoelastic fluids, Sci. Rep. **8**, 3618 (2018).

[79] C. Reichhardt and C. J. Olson Reichhardt, Active matter transport and jamming on disordered landscapes, Phys. Rev. E **90**, 012701 (2014).

[80] C. Reichhardt and C. J. O. Reichhardt, Negative differential mobility and trapping in active matter systems, J. Phys.: Condens. Matter **30**, 015404 (2018).

[81] C. Reichhardt and C.J.O. Reichhardt, Collective effects and pattern formation for directional locking of disks through obstacle arrays, Phys. Rev. E **102**, 022608 (2020).

[82] H. T. Nguyen, C. Reichhardt, and C. J. Olson Reichhardt, Clogging and jamming transitions in periodic obstacle arrays, Phys. Rev. E **95**, 030902(R) (2017).

[83] A. J. Liu and S. R. Nagel, Nonlinear dynamics - jamming is not just cool any more, Nature (London) **396**, 21 (1998).

[84] I. Zuriguel, D. R. Parisi, R. C. Hidalgo, C. Lozano, A. Janda, P. A. Gago, J. P. Peralta, L. M. Ferrer, L. A. Pugnaloni, E. Clément, D. Maza, I. Pagonabarraga, and A. Garcimartín, Clogging transition of many-particle systems flowing through bottlenecks, Sci. Rep. **4**, 7324 (2015).

[85] C. Barré and J. Talbot, Stochastic model of channel blocking with an inhomogeneous flux of entering particles, Europhys. Lett. **110**, 20005 (2015).

[86] R. L. Stoop and P. Tierno, Clogging and jamming of colloidal monolayers driven across disordered landscapes, Commun. Phys. **1**, 68 (2018).